

Stochastic Sampling of Operator Growth Dynamics

Ayush De,¹ Umberto Borla,¹ Xiangyu Cao,² and Snir Gazit^{1,3}

¹*Racah Institute of Physics, The Hebrew University of Jerusalem, Jerusalem 9190401, Israel*

²*Laboratoire de Physique de l'École normale supérieure, ENS, Université PSL, CNRS, Sorbonne Université, Université Paris Cité, F-75005 Paris, France*

³*The Fritz Haber Research Center for Molecular Dynamics, The Hebrew University of Jerusalem, Jerusalem 9190401, Israel*

(Dated: November 26, 2024)

We put forward a Monte Carlo algorithm that samples the Euclidean time operator growth dynamics at infinite temperature. Crucially, our approach is free from the numerical sign problem for a broad family of quantum many-body spin systems, allowing for numerically exact and unbiased calculations. We apply this methodological headway to study the high-frequency dynamics of the mixed-field quantum Ising model (QIM) in one and two dimensions. The resulting quantum dynamics display rapid thermalization, supporting the recently proposed operator growth hypothesis. Physically, our findings correspond to an exponential fall-off of generic response functions of local correlators at large frequencies. Remarkably, our calculations are sufficiently sensitive to detect subtle logarithmic corrections of the hypothesis in one dimension. In addition, in two dimensions, we uncover a non-trivial dynamical crossover between two large frequency decay rates. Lastly, we reveal spatio-temporal scaling laws associated with operator growth, which are found to be strongly affected by boundary contributions.

I. INTRODUCTION

Within the Heisenberg representation of quantum mechanics, the time evolution of operators is governed by their commutation relations with the Hamiltonian. Under generic many-body dynamics, local operators are expected to evolve into increasingly complex and non-local operator strings. This process of “operator growth” is equivalent to the scrambling of quantum information in complex systems and is closely related to quantum chaos. As such, understanding the precise properties of operator growth is a fundamental line of research that has driven a great amount of theoretical and experimental work [1–9]. It has direct links to the question of how the laws of quantum mechanics bring about thermalization or its failure in isolated systems [10–14]. It is also a useful tool for investigating the fate of information in a black hole and how to retrieve it [15–19].

In this context, an interesting way to quantify the rate of operator growth, besides the much studied out-of-time order correlator, is to examine the high-frequency regime of the spectral density $\Phi(\omega)$ associated with generic dynamical correlators [20]. Recently, Ref. [21] proposed an operator growth hypothesis that translates to an exponentially decaying large frequency tail

$$\Phi(\omega) \sim \exp(-|\omega|/\omega_0) \quad (1)$$

in generic many-body systems with finite local bandwidth. The energy scale ω_0 provides an upper bound to the Lyapunov exponent of out-of-time order correlators [21–23], and is thus an alternative measure of operator growth [24–30]. Crucially, this quantity is experimentally accessible [31], e.g., from the pre-thermalization time in a fast periodic drive [32].

Studying operator growth dynamics in concrete lattice models is particularly challenging due to the inher-

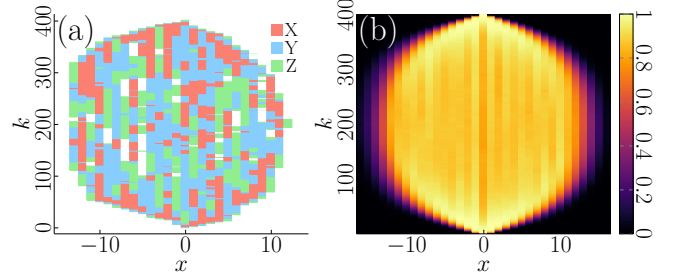


FIG. 1: (a) The operator growth history of the Z Pauli operator associated with a typical sequence belonging to \mathcal{S}_{2n} for $n = 200$ in Eq. (6) in the Pauli basis, for the mixed field QIM with Hamiltonian given in Eq. (9). The horizontal axis corresponds to space, and the vertical axis is generated by the temporal index k . The colors correspond to different Pauli operators at each site. (b) The average Pauli operator density across growth histories contributing to μ_{2n} for $n = 200$. Here, we only distinguish between the non-trivial Pauli operators and the identity. Both (a) and (b) have been extracted from our Monte Carlo simulations.

ent difficulty of simulating many-body quantum dynamics with classical resources, as reflected by the dynamical sign problem and the unbounded growth of entanglement entropy in thermalizing systems [33, 34]. From the perspective of the operator growth hypothesis, direct evidence is largely limited to large- N or semi-classical models [20, 23, 30, 35, 36] and brute-force numerics of small to intermediate system sizes that suffer from sizable finite size effects [37]. Although analytical bounds supporting the conjecture have been obtained for finite-dimensional systems [38, 39], these results are not satisfactory in that they do not provide an accurate estimate of ω_0 or the precise functional form of the spectral function. It is, therefore, desirable to devise efficient numerical schemes

that can reliably test the operator growth hypothesis.

In this article, we present a Monte Carlo method that samples the Euclidean time operator growth dynamics at infinite temperature in an unbiased and statistically exact manner. A unique feature of our formalism is that it tracks the Euclidean time evolution of *operators* (Fig. 1a) instead of the standard wave function approach that is common in conventional Quantum Monte Carlo (QMC) calculations. Crucially, our scheme does not suffer from the notorious numerical sign problem when applied to a broad family of lattice spin models of interest. By way of example, we employ our method to study the mixed-field Quantum Ising Model (QIM) in one- and two-dimensions and succeed in computing an order of magnitude more number of spectral function moments than what is accessible using brute force methods. This progress gives us direct access to high-frequency decay rates of the spectral tail. Furthermore, our results provide high-precision tests of the operator growth hypothesis. In particular, we pinpoint the subtle log-correction to Eq. (1) in 1D and unveil non-universal spectral features like an intriguing crossover between two high-frequency tails in 2D. Additionally, we determine the dynamical scaling properties of the operator support size.

II. CONSTRUCTING THE OPERATOR-SPACE PARTITION FUNCTION

In statistical physics, Monte Carlo schemes aim to tackle exponentially hard computational problems by mapping them to a sampling problem from a probability distribution. A useful starting point for constructing our partition function is to examine the auto-correlation function of a local operator, O , analytically continued to imaginary time $t = i\tau$:

$$\mathcal{C}(\tau) = \langle O(\tau)O(0) \rangle = (O|e^{\mathcal{L}\tau}|O). \quad (2)$$

Here, $(A|B) = \text{Tr}[A^\dagger B]/\text{Tr}[1]$ denotes the infinite-temperature scalar product on operator space. This enables a natural extension of the *bra-ket* notation to the operator Hilbert space, with $|O\rangle$ denoting the operator O and $\langle O|$ its vector dual O^\dagger . \mathcal{L} here is the Liouvillian super-operator associated with Hamiltonian H that transforms operator *kets* as $\mathcal{L}|O\rangle = |[H, O]\rangle$.

To make contact with the real frequency spectral density (and especially its large frequency tails) we Taylor expand $\mathcal{C}(\tau)$ about $\tau = 0$:

$$\mathcal{C}(\tau) = \sum_{n=0}^{\infty} \mu_{2n} \frac{\tau^{2n}}{(2n)!} \quad (3)$$

$$\mu_{2n} = (O|\mathcal{L}^{2n}|O) = \int \Phi(\omega) \omega^{2n} \frac{d\omega}{2\pi}. \quad (4)$$

In the last equation, we identify the Taylor expansion coefficients $\{\mu_{2n}\}$ with the moments of the spectral function $\Phi(\omega)$, defined as $\Phi(\omega) = \int d\tau e^{i\omega\tau} \langle O(\tau = it)O(0) \rangle$.

The moments thus encode information about the dynamics of the operator. An example of the high frequency part of spectral density associated with dynamics with the Z Pauli operator for the mixed-field QIM Hamiltonian Eq. (9) can be found in Eq. (12). In particular, an exponential tail of the spectral function (Eq. (1)) yields:

$$\mu_{2n} \simeq \left(\frac{2n\omega_0}{e} \right)^{2n} \quad (5)$$

for large n . The moments grow rapidly, such that $\mathcal{C}(\tau)$ converges only when $\tau < \tau_* = 1/\omega_0$, and has a pole at τ_* .

We aim to extract dynamical information by evaluating the moments. To map this calculation to a statistical mechanics problem, we express μ_{2n} as a sum over paths in operator space. Assuming local dynamics, we write $\mathcal{L} = \sum_{i,a} \mathcal{L}_{i,a}$, with $\{\mathcal{L}_{i,a}\}$ denoting local Liouvillian of type a acting on site i , as dictated by the underlying Hamiltonian, $H = \sum_{i,a} H_{i,a}$, with $\mathcal{L}_{i,a}|O\rangle = |[H_{i,a}, O]\rangle$. We then expand $(O|\mathcal{L}^{2n}|O)$ by introducing operator space resolution of identities between individual Liouvillians:

$$\mu_{2n} = \sum_{S_{2n}} \prod_{k=0}^{2n-1} \underbrace{(O_{k+1}|\mathcal{L}_{i_k, a_k} O_k)}_{W_{S_{2n}}}, \quad (6)$$

where the sum is over all local Liouvillian sequences, specified by $2n$ position-type pairs, $S_{2n} = \{(i_k, a_k)\}_{k=0}^{2n-1}$, with nonzero weight $W_{S_{2n}} \neq 0$. This construction implicitly defines operator histories between orthogonal operators ($O_0 = O, O_1, \dots, O_{2n} = O_0$). Eq. (6) imparts moments μ_{2n} the interpretation of a sum over all $2n$ long operator string *paths* generated by local Liouvillian sequences S_{2n} such that $O_0 = O_{2n} = O$. Fig. 1 illustrates this interpretation. We now consider the sum over all such operator paths up to $2n_{\max}$ in length:

$$G = \sum_{n=0}^{n_{\max}} \mu_{2n} = \sum_{n=0}^{n_{\max}} \sum_{S_{2n}} \prod_{k=0}^{2n-1} (O_{k+1}|\mathcal{L}_{i_k, a_k} O_k). \quad (7)$$

One can view G as a partition function associated with a probability distribution on n with $P(n) = \mu_{2n}/G$. In that case, the relative frequencies of sampling different values of n from $P(n)$ correspond to the relative magnitudes of the moments. This forms the central idea behind our sampling approach to computing the moments.

To tailor G for numerical Monte Carlo calculations, we make additional adjustments. Firstly, we make each operator string path $2n_{\max}$ long by inserting additional factors of identity Liouvillians. This results in duplication of paths which is compensated for by dividing by a binomial combinatorial factor. This step is reminiscent of the Stochastic Series Expansion (SSE) [40, 41], except that here, the configurations are in operator space with

transitions being generated by local Liouvillians as opposed to local Hamiltonians. Also in contrast to SSE, where the probability distribution of the expansion order rapidly decays away from its mean value (associated with the energy), here we will be interested in sampling all moments μ_{2n} and thus drawing samples from all orders of the expansion. Eq. (5) however suggests that the moments grow rapidly with n . Naively sampling from G would thus result in a highly skewed sampled histogram, with almost all samples coming from the large expansion orders close to n_{\max} . This would result in poor statistics for small to intermediate expansion orders. To counter this, we reweigh the moments by numerically determined factors w_n such that $w_n \mu_{2n}$ is of the same order of magnitude for all n . Accounting for the reweighting and the insertion of identity Liouvillians, our final generalized partition function now takes the form:

$$\mathcal{Z} = \sum_{n=0}^{n_{\max}} w_n \underbrace{\sum_{\mathcal{S}'_{2n}} \frac{1}{\binom{2n_{\max}}{2n}} \prod_{k=0}^{2n_{\max}-1} (O_{k+1} | \mathcal{L}_{i_k, a_k} O_k)}_{\mu_{2n}}. \quad (8)$$

Here, now, \mathcal{S}'_{2n} sums over all possible $2n_{\max}$ long Liouvillian sequences with $2n - 2n_{\max}$ Liouvillian identities and $\binom{2n_{\max}}{2n}$ is the aforementioned combinatorial binomial factor, compensating for the over counting introduced by identity Liouvillians.

It should be noted that in n_{\max} steps of commutation with a k local Hamiltonian, an operator can spatially grow by at most $(k-1) \times n_{\max}$ sites. Thus, for an operator O with finite support, a lattice with a linear spatial size larger than the sum of the support size of O and $(k-1) \times n_{\max}$ avoids any finite size effects in the calculation of the first n_{\max} moments.

An interesting observation is that for a particular choice of weights $w_n = \tau^{2n}/(2n)!$, \mathcal{Z} becomes the truncated Taylor expansion of $\mathcal{C}(\tau)$ from Eq. (3). For large n_{\max} , a choice of weights w_n that ensures a flat distribution across n would correspond to $\mathcal{C}(\tau)$ near criticality, $\tau \nearrow \tau_*$.

The weights W_S in Eq. (6) arise out of a product of commutations of operators and are thus generally non-positive even when the associated Hamiltonian problem is sign-problem free. Remarkably, for a class of nontrivial models, the sum in Eq. (6) contains strictly non-negative real terms, $W_S \geq 0$ [39], see further details in Section III. This class includes the mixed-field QIM, with the Hamiltonian:

$$H = -J \sum_{\langle i, j \rangle} Z_i Z_j - \sum_i (h^Z Z_i + h^X X_i). \quad (9)$$

Here, $\langle i, j \rangle$ define nearest neighbours on a hypercubic lattice and X_i, Z_i are the Pauli operators acting on sites i along the x, z spin axes, respectively. For such spin 1/2 models, Pauli strings, i.e. operators formed by the tensor product of local Pauli operators, are a convenient

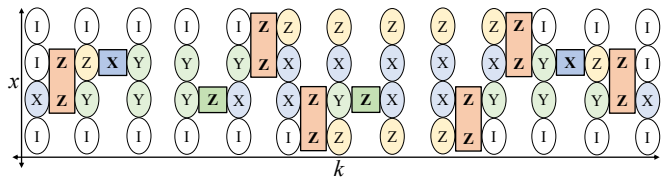


FIG. 2: A typical configuration contributing to \mathcal{Z} in Eq. (8) with $n = 4$, $n_{\max} = 5$ and $L = 4$ for the 1D mixed field QIM with Hamiltonian in Eq. (9). The horizontal and vertical axes correspond to the temporal index k and the spatial index i_k respectively. The sites are populated by the X, Y , and Z Pauli operators or the I (identity) operator. The temporal evolution is generated by Liouvillians of type $\mathcal{L}_Z, \mathcal{L}_{ZZ}$ and \mathcal{L}_X arising from the longitudinal field, bond and transverse field terms in the Hamiltonian respectively. The empty Liouvillian slots correspond to identity Liouvillians.

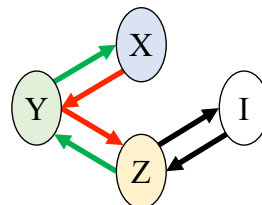


FIG. 3: The *operator state graph* of a site in the mixed field QIM Hamiltonian. The different states correspond to Pauli matrices, transitions between which are generated by local Liouvillians. The red and green arrows depict transitions arising from commutators with $+i$ and $-i$ phases respectively. The black arrows indicate transitions arising from matrix multiplications as can arise from \mathcal{L}_{ZZ} commutators and thus have no associated phase.

orthogonal basis choice for the resolution of Identities in Eq. (6). To avoid the sign problem, it is sufficient to assume that operator O_0 is itself a Pauli string. This then imparts the configurations in Eq. (8) a natural diagrammatic interpretation as a sum over configurations on a $D = d + 1$ dimensional space-time lattice with dimensions $L^d \times (2n_{\max} + 1)$. The lattice consists of Pauli strings spanning the spatial dimensions with the temporal dimension generated by local Liouvillians connecting Pauli strings. See Fig. 2.

III. SIGN PROBLEM RESOLUTION

To understand the resolution of the sign problem, it is useful to consider the *operator state graph* for a single site on the Pauli string lattice. Fig. 3 illustrates the same for the mixed field QIM. A site starts off in the state corresponding to the initial Pauli string O_0 . As the Pauli string evolves, the site traces a path in the *operator state graph*. The boundary conditions imposed in Eq. (6) however demand that each site return to the same state it began in. It can be seen from Fig. 3 that in the mixed field QIM, for a site to return to the same

state, it must encounter the same number of red transitions as green transitions, each associated with a phase factor of $+i$ and $-i$, respectively. Consequently, all operator paths will have the same number of $+i$ and $-i$ phase factors, cancelling out. Thus, all paths will have positive associated weights W_S .

More generally, the sign problem is prevented as long as there are no closed loops generated by red or green transitions in the *operator state graph*. In the specific case of the mixed field QIM, shown in Fig. 3, adding a $h^Y Y_i$ term to the Hamiltonian will enable additional red and green transitions between states X and Z (via commutations with the Y Pauli matrix). This will allow closed paths of the kind $X \rightarrow Y \rightarrow Z \rightarrow X$ with an i^3 phase to satisfy the fixed boundary conditions. A sufficient condition to prevent such closed loops (and consequently avoid the sign problem) is thus not to have all three Pauli matrices feature in the Hamiltonian expression. Beyond the mixed field QIM (which encompasses the Transverse Field Ising Model), the quantum XY model (in the absence of a Z field term) is another notable quantum spin model that does not exhibit a sign problem. On the contrary, the quantum Heisenberg model, with its bond terms involving all three Pauli matrices, will suffer from the sign problem.

IV. NUMERICAL METHODS AND OBSERVABLES

We now present a Monte Carlo sampling scheme for configurations in Eq. (8) for the mixed-field QIM. The moves are designed to traverse the configuration space by making local changes to the existing configuration. We describe them briefly here, and refer to Appendix A for technical details:

1. **add-drop** – allows switching between different n sectors by adding or removing a pair of identical local Liouvillians located on the same sites at two consecutive time slices.
2. **swap** – swaps two commuting Liouvillians at different time slices, without changing the moment order n . This move is proposed only if there are no non-commuting Liouvillians at intermediate time slices.
3. **interact** – here, two temporally consecutive \mathcal{L}_{ZZ} Liouvillians that share a single spatial site “interact” to create a pair of temporally consecutive \mathcal{L}_Z Liouvillians acting on next to nearest neighbour sites. This move allows accessing configurations with an odd number of \mathcal{L}_{ZZ} and \mathcal{L}_Z Liouvillians acting on a given site.

The weights w_n are determined using a reweighting approach similar to the Wang-Landau algorithm [42–44]. An initial guess choice is iteratively tuned until reaching

an approximately uniform distribution across the different μ_{2n} sectors. See Appendix A for implementation details.

Our key physical observable is the moments’ ratio:

$$r_n^2 := \frac{\mu_{2n+2}}{\mu_{2n}} = \frac{\langle \delta_{n',n+1} \rangle_{n'}}{\langle \delta_{n',n} \rangle_{n'}} \times \frac{w_n}{w_{n+1}} \quad (10)$$

In the above equation, averaging is carried out over the probability distribution $P(n')$ induced by \mathcal{Z} , where the Kronecker delta $\delta_{n',n}$ counts Monte Carlo events satisfying $n' = n$. The large frequency behavior of Eq. (1), predicts a linear growth of r_n with n , i.e. $r_n \simeq 2\omega_0 n$. In addition, the prefactor allows for a numerical estimation of the decay rate ω_0 .

To estimate the spatial extent of operator growth, we define the support size at time slice k as:

$$S_k = \langle \text{Volume}(B_k^d) \rangle. \quad (11)$$

Here, B_k^d is geometrically defined as the largest region in d dimensional space enclosed by non-trivial operators at temporal index k .

V. NUMERICAL RESULTS

In the following, we present Monte Carlo data for the Z operator dynamics associated with the spectral function $\Phi_{ZZ}(\omega) = \int d\tau e^{i\omega\tau} \langle Z(\tau = it)Z(0) \rangle$ in the mixed field QIM with the microscopic parameters $h^X = h^Z = J = 1$ in 1D and 2D and contrast them against brute force computations. The brute force calculations are performed by explicitly summing over all possible operator paths contributing to the moments, resulting in an unfavourable super-exponential scaling with the expansion order n . We begin our presentation by examining the 1D case. We recall that due to restricted dynamics in 1D, the linear growth of r_n receives a logarithmic correction such that $r_n \sim n/\log n$ [21, 32, 38, 45, 46]. In Fig. 4a, we depict r_n vs n . We first note the excellent agreement with brute force calculation as shown in the inset, serving as a non-trivial benchmark of our approach. Furthermore, we observe that the large n growth of r_n deviates from a linear trend. To pin down the source of this deviation and check whether it can be attributed to the aforementioned logarithmic correction in Fig. 4b, we plot $\Delta r_n \times \log(2n)$, where Δr_n is a numerical derivative extracted using the five-point stencil method. This quantity is expected to reach a plateau at large n with the logarithmic correction. Indeed, we find that only in the presence of the log multiplication, the desired plateau is obtained. By contrast, Δr_n asymptotically decays to zero due to the $1/\log(2n)$ factor. We note that this is the first numerically exact confirmation for the predicted log correction associated with the restricted 1D dynamics, as previous brute-force numerics cannot resolve this subtle functional dependence convincingly due to the limited number of accessible moments [21, 37, 47].

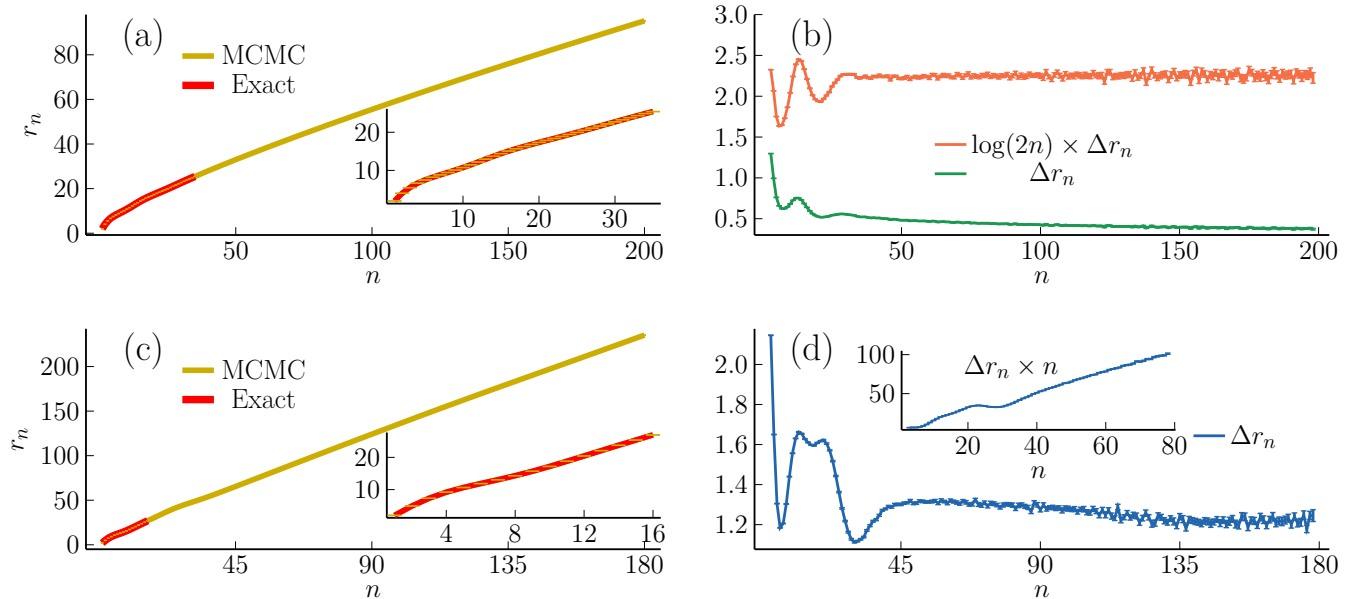


FIG. 4: (a) r_n vs n for the Z operator with $J = h^Z = h^X = 1$ in 1D. The inset zooms in on the comparison of our MCMC calculations for the first 35 moments with brute-force exact numerics. (b) Δr_n vs n for 1D. This asymptotically falls to zero. Multiplying by $\log(2n)$ recovers a constant plateau. (c) Same as (a) for 2D. The inset compares the first 16 moments against exact computation. (d) Δr_n vs n for 2D.

We now turn to study 2D systems. In Fig. 4c, we plot the evolution of r_n with the expansion order n . As before, we note the precise agreement with brute force computation, shown in the inset. Impressively, the stochastic approach allows access to the first 180 moments, as compared to brute force methods that are limited to the first 16 moments. We observe a clear linear trend of r_n , which is the first extensive test of the operator growth hypothesis in a concrete model beyond 1D systems.

In Fig. 4d, we plot Δr_n vs n . We observe that Δr_n settles into an intermediate false plateau $\Delta r_n \simeq 1.6J$ in the range $12 \lesssim n \lesssim 20$ before transitioning to its true asymptotic plateau of $\Delta r_n \simeq 1.24J$ that is truly established beyond $n \approx 40$. Since a constant value of Δr_n corresponds to an exponentially decaying spectral function with decay rate $\omega_0 = \Delta r_n/2$, the two-plateau structure allows us to infer that the spectral density features a crossover between two exponential tails. If we suppose

$$\Phi_{ZZ}(\omega) \sim \begin{cases} e^{-|\omega|/\omega_1} & |\omega| \lesssim \omega_c \\ e^{-|\omega|/\omega_2} & |\omega| \gtrsim \omega_c \end{cases} \quad (12)$$

where ω_1 and ω_2 are the decay rates and ω_c is the crossover scale. Using a saddle point approximation on Eq. (4), we find that

$$\Delta r_n \approx \begin{cases} 2\omega_1 & n \lesssim n_1 = \omega_c/2\omega_1 \\ 2\omega_2 & n \gtrsim n_2 = \omega_c/2\omega_2 \end{cases} \quad (13)$$

In particular, we have $n_1\omega_1 \approx n_2\omega_2 \approx \omega_c/2$. To show that our numerical results are consistent with Eq. (12), we plot $n\Delta r_n$ in the inset of Fig. 4d, and find $n_1 \approx 20$ and

$n_2 \approx 30$. This gives a remarkably large $\omega_c = 2n_1\omega_1 \approx 32J$. We note that the brute force calculations, limited to the first 16 moments, only capture the intermediate spectral decay rate ω_1 , missing the true asymptotic decay rate ω_2 entirely.

Owing to the thermal nature of the dynamics, we expect the large n behavior of r_n to be universal for typical local operators with a given set of model parameters. In Appendix B, we indeed see this anticipated behavior for boundary X operator, with $\log(2n)\Delta r_n \simeq 2.2(1)J$ and $\Delta r_n \simeq 1.26(4)J$ in 1D and 2D respectively, consistent with the plots here. We also find that the structure of the intermediate plateau as seen in 2D is not universal. Nevertheless, the asymptotic plateau value is reached only at a similar large value $n_2 \approx 40$. Correspondingly, the high-frequency tail of the spectral density is truly established only at a frequency that was numerically inaccessible before the present work.

VI. STATISTICAL MECHANICS PERSPECTIVE OF OPERATOR GROWTH

From the point of view of statistical mechanics, it is natural to examine geometric properties of the operator string configurations Fig. 1b. In particular, configurations with large n_{\max} describe the vicinity of the critical point $\tau \nearrow \tau_*$ in the expansion Eq. (3) (in 1D $\tau_* = \infty$ because of the log-correction). Therefore, these large n_{\max} configurations exhibit universal, scale-invariant behavior ubiquitous to continuous phase transitions.

To illustrate this point, we measured the average support size of operator strings against temporal index k in

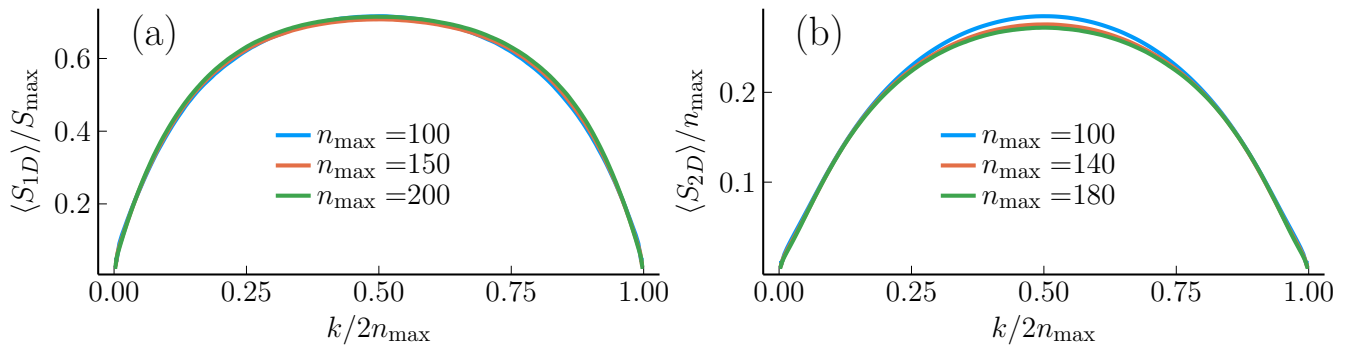


FIG. 5: Scaling collapse of the average operator support size (for the Z operator), as function of k , in 1D (a), where $S_{\max} := n_{\max}/\log n_{\max}$, and in 2D (b).

configurations with an increasing range of maximal expansion order n_{\max} . The results, plotted in Fig. 5, agree with the following scaling ansatz in the large n_{\max} limit:

$$\langle S_{2D} \rangle = n_{\max} f_{2D}(k/2n_{\max}), \quad (14a)$$

$$\langle S_{1D} \rangle = \frac{n_{\max}}{\log(n_{\max})} f_{1D}(k/2n_{\max}) \quad (14b)$$

where f_{2D} and f_{1D} are scaling functions, which capture the evolution of the operator size growth to an n_{\max} -dependent maximum (and then decrease) in terms of rescaled time $k/2n_{\max}$ and size S/S_{\max} . The scaling of S_{\max} with respect to n_{\max} is expected to be universal, and depend on the dimension. In 2D and higher dimensions, $S_{\max} \sim n_{\max}$. This is the only asymptotics compatible with the universal moment growth in Eq. (5). Indeed, the slow convergence to the scaling collapse echos the late establishment of the universal growth observed above. In 1D, there is a log-correction $S_{\max} = n_{\max}/\log(n_{\max})$. This has the same geometric origin as the log-correction to the moment growth: the operator can only grow at the two extremities, which is a severe entropy penalty. Therefore the dominant contributions are a compromise: the operator grows less in order to “scramble” more in the bulk, and S_{\max} is the optimal scaling form of the maximal size [38, 45]. Finally, the scaling functions f_{2D} and f_{1D} are independent of the operator, which corresponds to the boundary condition of the partition sum. To what extent they depend on the Hamiltonian is an interesting question.

VII. DISCUSSION

We conclude our presentation by flagging several research directions motivated by our results. Our approach can be extended to models whose associated Liouvillian dynamics are expressed as sign problem-free sums. The quantum XY model is a notable example [39], which crucially admits a global $U(1)$ symmetry and hence can provide access to transport properties of conserved charges [48, 49]. The presence of disorder is also compatible with

our method, it will be interesting to investigate signatures of Many-Body Localization in the evolution of operator strings. Another important direction is extracting real frequency dynamical spectral functions away from the high-frequency limit, as can, in principle, be via Lanczos coefficients expressed in terms of moment ratios [50–52]. We note that the latter might suffer from high sensitivity to statistical noise and may require an improvement on current algorithms. Nevertheless, seeing how our Monte Carlo method fares against the existing techniques [53–55] will be an interesting line of enquiry. Lastly, we expect the support size scaling functions to be universal and valid for a generic class of chaotic Hamiltonians, and predicting them theoretically is an intriguing open question. We leave the aforementioned possibilities to future efforts.

ACKNOWLEDGMENTS

We thank Ehud Altman, Assa Auerbach, Thomas Scaffidi and Daniel Parker for fruitful discussions and comments. S.G. acknowledges support from the Israel Science Foundation (ISF) Grant no. 586/22 and the US–Israel Binational Science Foundation (BSF) Grant no. 2020264. U.B. acknowledges support from the Israel Academy of Sciences and Humanities through the Excellence Fellowship for International Postdoctoral Researchers. Computational resources were provided by the Intel Labs Academic Compute Environment and the Fritz Haber Center for Molecular Dynamics, Hebrew University. X.C. acknowledges support from a France-Berkeley Fund grant (Project #24.2023).

Appendix A: The Monte Carlo Algorithm

In this section, we outline our Markov chain Monte Carlo (MCMC) sampling algorithm. We first discuss the re-weighting procedure used in Eq. (8). The weights $\{w_n\}$ may be initialized as $w_n = 1/(J^{2n}(2n!))$. This choice is useful as it is an upper bound to the radius of converge of the μ_{2n} sequence [39]. In practice one only

needs to keep track of weight ratios between consecutive n sectors w_n/w_{n+1} . The reweighting procedure works iteratively. At each step, we take N samples and determine the number of times c_n that each sector is visited by the MCMC. We define c_n as:

$$c_n = \sum_{i=1}^N \delta_{n,n_i}. \quad (\text{A1})$$

For a flat distribution, one expects $c_n \sim (n_{\max} + 1)/N$. To bias our distribution in this direction, we update the weights by setting $w_n \rightarrow w_n N / (c_n (n_{\max} + 1))$. The corresponding stored weight ratios get updated as: $w_n/w_{n+1} \rightarrow (w_n/w_{n+1}) \times (c_{n+1}/c_n)$. This assignment penalizes sectors with $c_n > (n_{\max} + 1)/N$ by reducing their weight and reinforces weights for sectors with $c_n < (n_{\max} + 1)/N$. This procedure is carried out repeatedly until an approximately flat distribution is obtained.

We now move our discussion towards the Monte Carlo moves. The moves are designed to ensure ergodicity while only making local changes to the configuration space. Below, we discuss the three classes of moves: **add-drop**, **swap** and **interact**. For the rest of this section, we will work with a $d + 1$ dimensional lattice with length L and $2n_{\max} + 1$ temporal slices. The temporal axis is pictured in the vertical direction. While the schematic diagrams show the moves on a $d = 1$ lattice, they generally also apply to higher dimensional cases. We will point out subtleties pertaining to $d > 1$ dimensions when appropriate.

1. Add-drop

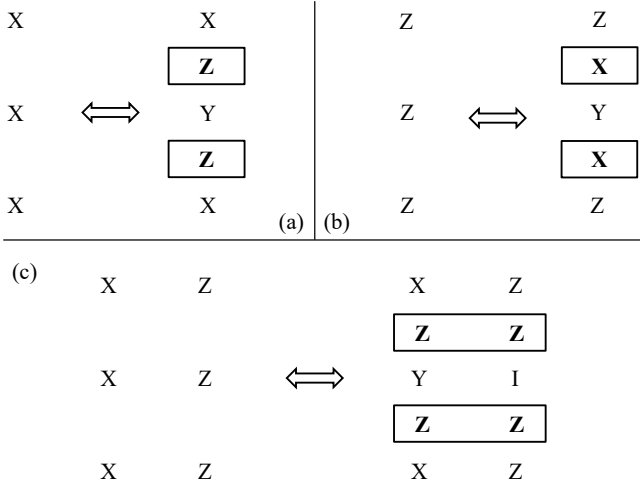


FIG. 6: Illustration of the **add-drop** moves with (a) \mathcal{L}_Z Liouvillians (b) \mathcal{L}_X Liouvillians (c) \mathcal{L}_{ZZ} Liouvillians. The temporal direction is vertical.

The **add-drop** move is designed to allow transitioning between the different n sectors by adding and removing a pair of identical local Liouvillians. As illustrated in Fig. 6, the move is defined as follows:

1. Randomly choose a time slice with uniform probability.
2. If the local Liouvillians occupying both sides of the time slice are identical, propose to remove both.
3. Else, if the Liouvillian slots on both sides are unoccupied, randomly choose a site with uniform probability and propose to add a pair of identical Liouvillians onto the unoccupied slots at that site.

We now determine the transition probabilities. Let i be a configuration in the $n - 1$ sector with the $(k - 1)$ -th and k -th Liouvillian slots unoccupied. Let f be a configuration in the n sector that is identical to i except with these slots occupied at site r by Liouvillians $\mathcal{L}_{r_{k-1}, a_{k-1}} = \mathcal{L}_{r_k, a_k} =: \mathcal{L}_{r, a}$. The two configurations are thus related by an add-drop move. Based on Eq. (8), detailed balance imposes the constraint:

$$\begin{aligned} \frac{T_{i \rightarrow f} A_{i \rightarrow f}}{T_{f \rightarrow i} A_{f \rightarrow i}} &= \frac{P_f}{P_i} \\ &= \frac{w_n (O_{k-1} | \mathcal{L}_{r, a} | O_k) (O_k | \mathcal{L}_{r, a} | O_{k+1}) (2n)(2n-1)}{w_{n-1} (2n_{\max} - 2n + 2)(2n_{\max} - 2n + 1)}. \end{aligned} \quad (\text{A2})$$

Here, P_i, P_f are associated probabilities for states i, f ; $T_{i \rightarrow f}, T_{f \rightarrow i}$ are probabilities to propose the add/drop transitions and $A_{i \rightarrow f}, A_{f \rightarrow i}$ are the acceptance probabilities for the moves. Now, proposing an **add** operation involves choosing a time slice, followed by choosing a site and then choosing a Liouvillian type; proposing a **drop** amounts to simply choosing a time slice. Therefore the proposition probabilities are

$$\begin{aligned} T_{i \rightarrow f} &= \frac{1}{2n_{\max} + 1} \times \frac{1}{L^d} \times \frac{(O_{k-1} | \mathcal{L}_{r, a} | O_k) (O_k | \mathcal{L}_{r, a} | O_{k+1})}{\sigma}, \\ T_{f \rightarrow i} &= \frac{1}{2n_{\max} + 1}. \end{aligned} \quad (\text{A3})$$

where we denoted $\sigma = 4(dJ^2 + (h^X)^2 + (h^Z)^2)$ as the sum of weights of all possible Liouvillians at a site. Therefore, the following ‘‘Metropolis’’ acceptance rates satisfy detailed balance:

$$\begin{aligned} A_{i \rightarrow f} &= \min \left(1, \frac{w_n L^d \sigma (2n)(2n-1)}{w_{n-1} (2n_{\max} - 2n + 2)(2n_{\max} - 2n + 1)} \right), \\ A_{f \rightarrow i} &= \min \left(1, \frac{w_{n-1} (2n_{\max} - 2n + 2)(2n_{\max} - 2n + 1)}{w_n L^d \sigma (2n)(2n-1)} \right). \end{aligned} \quad (\text{A4})$$

2. Swap

The **swap** move permutes through different configurations in the same n sector using the commutation property of Liouvillian pairs, see Fig. 7 for an illustration. Before discussing the steps, we first define the notion of

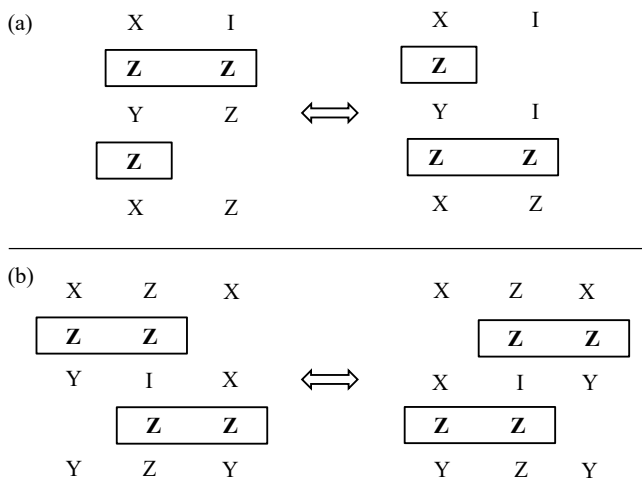


FIG. 7: Illustration of the **swap** move. We show two examples of Liouvillians that commute with each other: (a) \mathcal{L}_Z and \mathcal{L}_{ZZ} Liouvillians sharing a site. (b) Two \mathcal{L}_{ZZ} Liouvillians sharing just one site. In addition to (a) and (b), identical Liouvillians (those of the same kind, on the same site; and along the same axis in case of \mathcal{L}_{ZZ}) and those on different sites with no overlap, trivially commute.

“ceiling” and “floor”. The ceiling (floor) of a Liouvillian is the temporally closest Liouvillian above (below, respectively) it which doesn’t commute with it. If a non-commuting Liouvillian is lacking, the ceiling/floor is then defined to be the initial/final temporal boundary. Now, the **swap** steps are as follows:

1. Randomly, with uniform probability, choose a Liouvillian.
2. Randomly, with uniform probability, choose a second Liouvillian slot amongst those lying between the ceiling and floor of the first Liouvillian.
3. If the newly chosen slot is empty, remove the Liouvillian from its existing slot and place it in the new slot.
4. Otherwise, that is, if the slot is occupied by another Liouvillian, check whether the ceiling and floor of this second Liouvillian lie at an intermediate temporal index between the indices of the two Liouvillians. If that is not the case, swap the two Liouvillians.

Since the **swap** moves involve no weight change and everything is sampled uniformly, it satisfies detailed balance automatically, that is, with 100% acceptance rate.

3. Interact

The **add-drop** move only allows Liouvillians to exist on a site in pairs. This can however miss configurations with

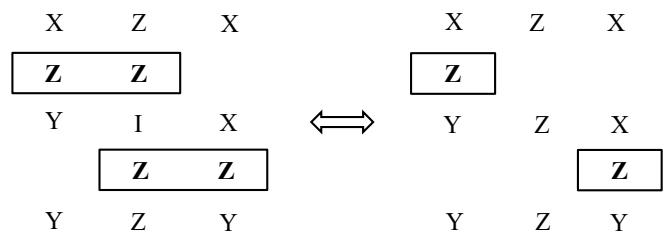


FIG. 8: Illustration of the **interact** move. Two \mathcal{L}_{ZZ} Liouvillians sharing only one site may “interact” to give a pair of \mathcal{L}_Z Liouvillians situated on next to nearest neighbour sites.

an odd number of bond Liouvillians on a site. To enable this we introduce the **interact** move, as illustrated in Fig. 8. It is to be noted that for $d > 1$, the two interacting bonds can be along different spatial axes. In such cases, two different \mathcal{L}_{ZZ} pair configurations can map to the same \mathcal{L}_Z pair configuration. This needs to be accounted for in detailed balance.

The interaction is implemented as:

1. Randomly choose a time slice with uniform probability.
2. If the Liouvillian on both sides of the time slice are of type \mathcal{L}_{ZZ} and share exactly one site, check if the shared site has a Z or I operator on it. If so, replace the \mathcal{L}_{ZZ} Liouvillians with \mathcal{L}_Z Liouvillians as in Fig. 8.
3. If the Liouvillian slots on both sides host \mathcal{L}_Z Liouvillians placed at next to nearest neighbour sites, check if their common nearest neighbouring site has a Z or I operator. If this is the case, replace the \mathcal{L}_Z Liouvillians with \mathcal{L}_{ZZ} Liouvillians as in Fig. 8.

Now, we derive the transition probabilities. Let i be a configuration with \mathcal{L}_{ZZ} Liouvillians on the $k-1$ -th and k -th time slots sharing a single site r . Let f be the configuration related to i by the **interact** move, hosting two \mathcal{L}_Z Liouvillians. Now, detailed balance implies:

$$\frac{T_{i \rightarrow f} A_{i \rightarrow f}}{T_{f \rightarrow i} A_{f \rightarrow i}} = \frac{P_f}{P_i} = \frac{(h^Z)^2}{J^2} \quad (\text{A5})$$

where P_i, P_f are the respective weights, $T_{i \rightarrow f}, T_{f \rightarrow i}$ are proposition probabilities and $A_{i \rightarrow f}, A_{f \rightarrow i}$ the acceptance probabilities. We claim that the proposition probabilities are as follows:

$$T_{i \rightarrow f} = \frac{1}{2n_{\max} + 1}, \quad T_{f \rightarrow i} = \frac{1}{(2n_{\max} + 1)\alpha}, \quad (\text{A6})$$

where $\alpha = 2$ if the \mathcal{L}_{ZZ} Liouvillians in configuration i are along different spatial directions (otherwise, $\alpha = 1$). This is because, proposing a $\mathcal{L}_{ZZ} \rightarrow \mathcal{L}_Z$ **interact** move amounts to choosing a time slice. Meanwhile, to specify a $\mathcal{L}_Z \rightarrow \mathcal{L}_{ZZ}$ **interact** move, we need to choose a time

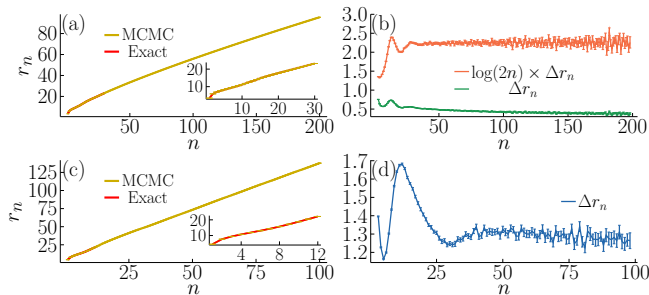


FIG. 9: (a) r_n vs n for the X operator with $J = h^Z = h^X = 1$ in 1D. The inset focuses in on the first 30 moments, comparing our MCMC with exact numerics. (b) Δr_n and $\log(2n)\Delta r_n$ vs n for 1D. (c) Same as (a) for 2D. The inset has the first 12 moments. (d) Δr_n vs n for 2D.

slice, and then pick a common neighboring site among the α choices. Therefore, the following acceptance rates fulfill detailed balance:

$$A_{i \rightarrow f} = \min\left(1, \frac{(h^Z)^2}{\alpha J^2}\right), \quad A_{f \rightarrow i} = \min\left(1, \frac{\alpha J^2}{(h^Z)^2}\right). \quad (\text{A7})$$

Appendix B: X Correlation Function

The statistical nature of infinite temperature operator growth dynamics in non-integrable systems like the mixed field QIM implies that local operators should typically give rise to the same generic behaviour at a large enough order n . Based on the Operator Growth Hypothesis [21], one expects local operators to asymptotically grow linearly with the same slope. To check this, we compute the same plots as Fig. 3 in the main text but for the X operator in Fig. 9. We see that for 1D $\log(2n)\Delta r_n$ vs n again gives us a constant curve $\log(2n)\Delta r_n \simeq 2.2(1)J$, the same as the Z operator in the main text. Similarly, in 2D we again get a plot consistent with linear growth with slope $\simeq 1.26(4)J$. Another point to note is the non-universal nature of the intermediate plateau in the 2D Δr_n vs n plot. We see that here the plateau is much narrower than the one for the Z operator as shown in the main text.

Appendix C: Additional move for the TFIM Limit

In the $h^Z = 0$ limit, the **interact** move breaks down. This is not a problem in 1D as configurations with an

odd number of identical \mathcal{L}_{ZZ} Liouvillians also require the presence of \mathcal{L}_Z Liouvillians and thus do not exist in this limit. For $d > 1$ it is possible for configurations to have an odd number of identical \mathcal{L}_{ZZ} Liouvillians without \mathcal{L}_Z Liouvillians. Fig. 10 shows a simple example with \mathcal{L}_{ZZ} Liouvillians *looping* around a plaquette, satisfying the boundary conditions. Note that each site hosts just one \mathcal{L}_{ZZ} Liouvillian of a kind. One can generate larger

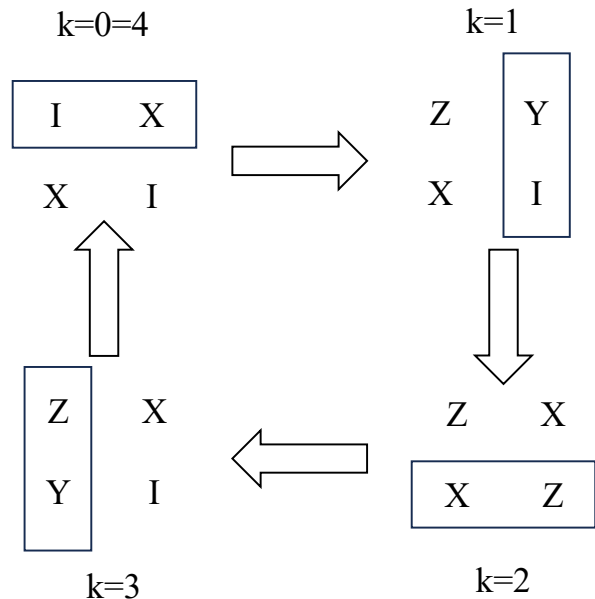


FIG. 10: An example of a configuration in the $n = 2$ sector that requires the **interact** move to be generated. Temporal slices of the 2D lattice are indexed by k . The first temporal slice is identical to the last because of the fixed boundary conditions. The \mathcal{L}_{ZZ} Liouvillians, shown as rectangular boxes, transform local Pauli operators between slices.

loops by removing \mathcal{L}_{ZZ} pairs on the common edges of overlapping smaller *loops* using **add-drop**.

To access this part of the configuration space in absence of **interact** we propose the **rotate** move. Fig. 11 shows that it is possible to rotate two parallel \mathcal{L}_{ZZ} Liouvillians sharing a plaquette to get another pair of parallel \mathcal{L}_{ZZ} Liouvillians on the same plaquette while maintaining the same boundaries. Detailed balance for this move should be trivial as the involved configurations have the same weight and thus the Metropolis acceptance rate is 100%. It can be seen that a combination of **add-drop** and **rotate** can generate the configuration in Fig. 10. We benchmark this move against exact numerics in Fig. 12.

- [1] B. Swingle, G. Bentsen, M. Schleier-Smith, and P. Hayden, Measuring the scrambling of quantum information, *Phys. Rev. A* **94**, 040302(R) (2016).
 [2] A. Nahum, S. Vijay, and J. Haah, Operator spreading in random unitary circuits, *Phys. Rev. X* **8**, 021014 (2018).

- [3] V. Khemani, A. Vishwanath, and D. A. Huse, Operator spreading and the emergence of dissipative hydrodynamics under unitary evolution with conservation laws, *Phys. Rev. X* **8**, 031057 (2018).
 [4] V. Khemani, D. A. Huse, and A. Nahum, Velocity-

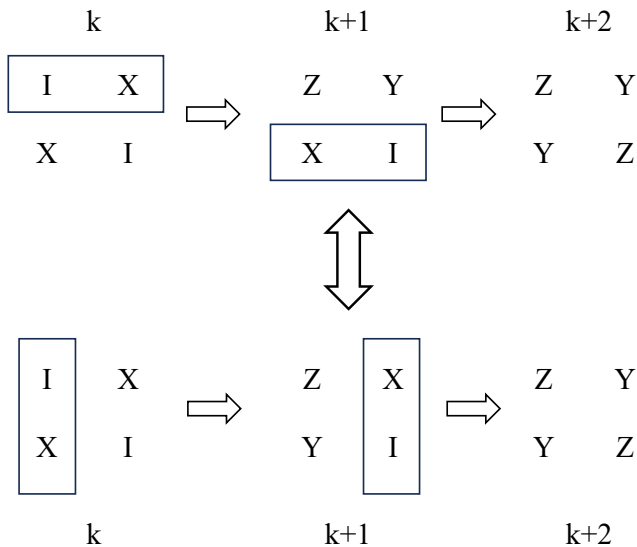


FIG. 11: Section of two configurations connected by the `rotate` move on a 2D lattice. k corresponds to the temporal index. Note that both configurations have the same temporal boundaries, implying the local nature of the move.

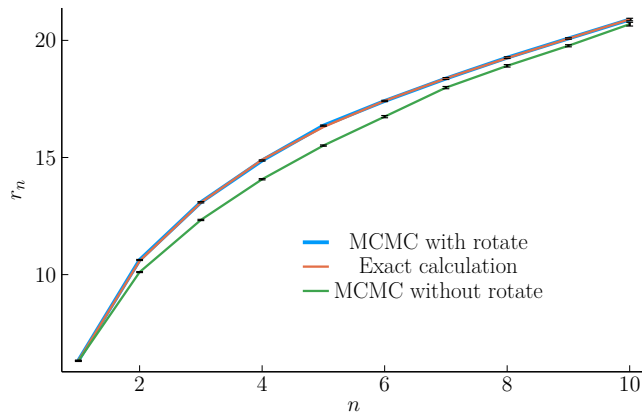


FIG. 12: Comparing our MCMC equipped with and without the `rotate` move against exact computations for the 2D TFIM with the same boundary operator as in Fig. 10.

dependent lyapunov exponents in many-body quantum, semiclassical, and classical chaos, *Phys. Rev. B* **98**, 144304(R) (2018).

- [5] S. Gopalakrishnan, D. A. Huse, V. Khemani, and R. Vasseur, Hydrodynamics of operator spreading and quasiparticle diffusion in interacting integrable systems, *Phys. Rev. B* **98**, 220303 (2018).
- [6] X.-L. Qi and A. Streicher, Quantum epidemiology: operator growth, thermal effects, and syk, *Journal of High Energy Physics* **2019**, 12 (2019).
- [7] D. A. Roberts, D. Stanford, and A. Streicher, Operator growth in the syk model, *Journal of High Energy Physics* **2018**, 122 (2018).
- [8] S. Xu and B. Swingle, Accessing scrambling using matrix product operators, *Nature Physics* **16**, 199 (2020).

- [9] B. Swingle, Unscrambling the physics of out-of-time-order correlators, *Nature Physics* **14**, 988 (2018).
- [10] J. M. Deutsch, Quantum statistical mechanics in a closed system, *Phys. Rev. A* **43**, 2046 (1991).
- [11] M. Srednicki, Chaos and quantum thermalization, *Phys. Rev. E* **50**, 888 (1994).
- [12] L. D'Alessio, Y. Kafri, A. Polkovnikov, and M. Rigol, From quantum chaos and eigenstate thermalization to statistical mechanics and thermodynamics, *Advances in Physics* **65**, 239 (2016).
- [13] D. A. Abanin, E. Altman, I. Bloch, and M. Serbyn, Colloquium: Many-body localization, thermalization, and entanglement, *Rev. Mod. Phys.* **91**, 021001 (2019).
- [14] R. Nandkishore and D. A. Huse, Many-body localization and thermalization in quantum statistical mechanics, *Annual Review of Condensed Matter Physics* **6**, 15 (2015).
- [15] Y. Sekino and L. Susskind, Fast scramblers, *Journal of High Energy Physics* **2008**, 065 (2008).
- [16] S. H. Shenker and D. Stanford, Black holes and the butterfly effect, *Journal of High Energy Physics* **2014**, 67 (2014).
- [17] J. Maldacena, S. H. Shenker, and D. Stanford, A bound on chaos, *Journal of High Energy Physics* **2016**, 106 (2016).
- [18] A. R. Brown, H. Gharibyan, S. Leichenauer, H. W. Lin, S. Nezami, G. Salton, L. Susskind, B. Swingle, and M. Walter, Quantum gravity in the lab. i. teleportation by size and traversable wormholes, *PRX Quantum* **4**, 010320 (2023).
- [19] T. Schuster, B. Kobrin, P. Gao, I. Cong, E. T. Khabiboulline, N. M. Linke, M. D. Lukin, C. Monroe, B. Yoshida, and N. Y. Yao, Many-body quantum teleportation via operator spreading in the traversable wormhole protocol, *Phys. Rev. X* **12**, 031013 (2022).
- [20] T. A. Elsayed, B. Hess, and B. V. Fine, Signatures of chaos in time series generated by many-spin systems at high temperatures, *Phys. Rev. E* **90**, 022910 (2014).
- [21] D. E. Parker, X. Cao, A. Avdoshkin, T. Scaffidi, and E. Altman, A universal operator growth hypothesis, *Phys. Rev. X* **9**, 041017 (2019).
- [22] C. Murthy and M. Srednicki, Bounds on chaos from the eigenstate thermalization hypothesis, *Phys. Rev. Lett.* **123**, 230606 (2019).
- [23] Y. Gu, A. Kitaev, and P. Zhang, A two-way approach to out-of-time-order correlators, *Journal of High Energy Physics* **2022**, 133 (2022).
- [24] J. L. F. Barbón, E. Rabinovici, R. Shir, and R. Sinha, On the evolution of operator complexity beyond scrambling, *Journal of High Energy Physics* **2019**, 264 (2019).
- [25] E. Rabinovici, A. Sánchez-Garrido, R. Shir, and J. Sonner, Operator complexity: a journey to the edge of krylov space, *Journal of High Energy Physics* **2021**, 62 (2021).
- [26] E. Rabinovici, A. Sánchez-Garrido, R. Shir, and J. Sonner, Krylov complexity from integrability to chaos, *Journal of High Energy Physics* **2022**, 151 (2022).
- [27] A. Avdoshkin and A. Dymarsky, Euclidean operator growth and quantum chaos, *Phys. Rev. Res.* **2**, 043234 (2020).
- [28] A. Dymarsky and M. Smolkin, Krylov complexity in conformal field theory, *Phys. Rev. D* **104**, L081702 (2021).
- [29] A. Avdoshkin, A. Dymarsky, and M. Smolkin, Krylov complexity in quantum field theory, and beyond, [arXiv:2212.14429](https://arxiv.org/abs/2212.14429) (2022).
- [30] S.-K. Jian, B. Swingle, and Z.-Y. Xian, Complexity

- growth of operators in the syk model and in jt gravity, *Journal of High Energy Physics* **2021**, 14 (2021).
- [31] A. Rubio-Abadal, M. Ippoliti, S. Hollerith, D. Wei, J. Rui, S. L. Sondhi, V. Khemani, C. Gross, and I. Bloch, Floquet prethermalization in a bose-hubbard system, *Phys. Rev. X* **10**, 021044 (2020).
- [32] D. Abanin, W. De Roeck, W. W. Ho, and F. Huveneers, A rigorous theory of many-body prethermalization for periodically driven and closed quantum systems, *Communications in Mathematical Physics* **354**, 809 (2017).
- [33] H. Kim and D. A. Huse, Ballistic spreading of entanglement in a diffusive nonintegrable system, *Phys. Rev. Lett.* **111**, 127205 (2013).
- [34] L. Mühlbacher and E. Rabani, Real-time path integral approach to nonequilibrium many-body quantum systems, *Phys. Rev. Lett.* **100**, 176403 (2008).
- [35] B. Bhattacharjee, P. Nandy, and T. Pathak, Krylov complexity in large q and double-scaled syk model, *Journal of High Energy Physics* **2023**, 99 (2023).
- [36] B. Bhattacharjee, X. Cao, P. Nandy, and T. Pathak, Krylov complexity in saddle-dominated scrambling, *Journal of High Energy Physics* **2022**, 174 (2022).
- [37] R. Heveling, J. Wang, and J. Gemmer, Numerically probing the universal operator growth hypothesis, *Phys. Rev. E* **106**, 014152 (2022).
- [38] G. Bouch, Complex-time singularity and locality estimates for quantum lattice systems, *Journal of Mathematical Physics* **56**, 123303 (2015).
- [39] X. Cao, A statistical mechanism for operator growth, *Journal of Physics A: Mathematical and Theoretical* **54**, 144001 (2021).
- [40] A. W. Sandvik and J. Kurkijärvi, Quantum monte carlo simulation method for spin systems, *Phys. Rev. B* **43**, 5950 (1991).
- [41] A. W. Sandvik, Computational Studies of Quantum Spin Systems, *AIP Conference Proceedings* **1297**, 135 (2010).
- [42] F. Wang and D. P. Landau, Efficient, multiple-range random walk algorithm to calculate the density of states, *Phys. Rev. Lett.* **86**, 2050 (2001).
- [43] M. Troyer, S. Wessel, and F. Alet, Flat histogram methods for quantum systems: Algorithms to overcome tunneling problems and calculate the free energy, *Phys. Rev. Lett.* **90**, 120201 (2003).
- [44] R. E. Belardinelli, S. Manzi, and V. D. Pereyra, Analysis of the convergence of the $1/t$ and wang-landau algorithms in the calculation of multidimensional integrals, *Phys. Rev. E* **78**, 067701 (2008).
- [45] H. Araki, Gibbs states of a one dimensional quantum lattice, *Communications in Mathematical Physics* **14**, 120 (1969).
- [46] P. Ponte, Z. Papić, F. Huveneers, and D. A. Abanin, Many-body localization in periodically driven systems, *Phys. Rev. Lett.* **114**, 140401 (2015).
- [47] J. D. Noh, Operator growth in the transverse-field ising spin chain with integrability-breaking longitudinal field, *Phys. Rev. E* **104**, 034112 (2021).
- [48] N. H. Lindner and A. Auerbach, Conductivity of hard core bosons: A paradigm of a bad metal, *Phys. Rev. B* **81**, 054512 (2010).
- [49] S. Bhattacharyya, A. De, S. Gazit, and A. Auerbach, Metallic transport of hard-core bosons, *Phys. Rev. B* **109**, 035117 (2024).
- [50] V. S. Viswanath and G. Müller, Recursion method in quantum spin dynamics: The art of terminating a continued fraction, *Journal of Applied Physics* **67**, 5486 (1990).
- [51] V. Viswanath and G. Müller, *The Recursion Method: Application to Many-Body Dynamics*, Lecture Notes in Physics Monographs (Springer Berlin Heidelberg, 2008).
- [52] I. Khait, S. Gazit, N. Y. Yao, and A. Auerbach, Spin transport of weakly disordered heisenberg chain at infinite temperature, *Phys. Rev. B* **93**, 224205 (2016).
- [53] T. Rakovszky, C. W. von Keyserlingk, and F. Pollmann, Dissipation-assisted operator evolution method for capturing hydrodynamic transport, *Phys. Rev. B* **105**, 075131 (2022).
- [54] J. Wang, M. H. Lamann, R. Steinigeweg, and J. Gemmer, Diffusion constants from the recursion method, *Phys. Rev. B* **110**, 104413 (2024).
- [55] F. Uskov and O. Lychkovskiy, Quantum dynamics in one and two dimensions via the recursion method, *Phys. Rev. B* **109**, L140301 (2024).